On data-driven augmentation of low-resolution ocean model dynamics

E.A. Ryzhov [a,*], D. Kondrashov [b,c], N. Agarwal [a], P.S. Berloff [a]

[a] *Department of Mathematics, Imperial College London, London, SW7 2AZ, UK*
[b] *Department of Atmospheric and Oceanic Sciences, University of California, Los Angeles, CA 90095, USA*
[c] *Institute of Applied Physics of the Russian Academy of Sciences, 603950, Nizhny Novgorod, Russia*

ARTICLE INFO

ABSTRACT

The problem of augmenting low-resolution ocean circulation models with the information extracted from the data relevant to the unresolved subgrid processes is addressed. A highly nonlinear model of eddy-resolving oceanic circulation – quasigeostrophic wind-driven double gyres – is considered. The model solutions are characterized by a vigorous dynamic coupling between the resolved large-scale and small-scale (eddy) flow features. This solution provides the data for augmenting the low-resolution model with the same configuration. The eddy forcing field, which contains the essential information about coupling between the large and eddy scales, is obtained, modified, coarse-grained and added to augment the low-resolution model. The implemented modification involves novel data-adaptive harmonic decomposition analysis and dynamical constraining based on the low-resolution nonlinear advection operator. The resulting augmentation of the low-resolution model significantly improves the solution, including its time-mean circulation and low-frequency variability. This result also paves the way for a systematic data-driven emulation of unresolved and under-resolved scales of motion.

1. Introduction

Ocean modelling is a challenging problem, because model solutions are usually critically sensitive to the spatial numerical grid resolutions. If the solution lacks the dynamics produced by unresolved sub-grid processes, then the resolved processes are also affected due to the involved nonlinearity. A notable example is oceanic mesoscale eddies which not only affect the large-scale circulation (Berloff and McWilliams, 1999; Kravtsov et al., 2006; Berloff et al., 2007; Shevchenko et al., 2016) but also facilitate material transport and mixing (Chelton et al., 2007, 2011; Samelson, 2013; Zhang et al., 2014; Dong et al., 2014; Abernathey and Haller, 2018; Liu et al., 2018). Therefore, it is important to parameterize the eddy effects in non-eddy-resolving and eddy-permitting models.

Different approaches to the eddy parameterization can be sorted into two main categories: deterministic and stochastic. The former approach adds to the governing equations some deterministic correction terms with clear physical meanings (Holloway, 1987; Gent and McWilliams, 1990; Frederiksen and Davies, 1997; Frederiksen, 1999; Griffies et al., 2000; Jansen and Held, 2014; O´Kane and Frederiksen, 2008; Frederiksen et al., 2012; Kitsios et al., 2013; Grooms et al., 2015; Jansen et al., 2015; Zanna et al., 2017; Mak et al., 2017, 2018; Berloff, 2018; Danilov et al., 2019; Juricke et al., 2019). The main problem

here is that it is difficult to account separately for all the important unresolved physical processes, given that dynamical interactions between these processes are nonlinear and structurally complex. The stochastic approach introduces randomness to the governing equations (Berloff, 2005b; Crommelin and Vanden-Eijnden, 2008; Zidikheri and Frederiksen, 2010a,b; Porta Mana and Zanna, 2014; Samelson et al., 2016; Zacharuk et al., 2018; Bachman, 2019), and statistical laws defining this randomness vary across different problems and often include complicated and poorly constrained correlations in time and space. Instead of looking for the theoretical constraints, one may resort to the data-driven approach based on *a priori* analysis of the existing data. This analysis can provide relevant spatial and temporal correlations, and help to augment the low-resolution prognostic model with the inferred statistical information. The *a priori* given data may come from different sources; such as high-resolution model solutions or real observations.

The present study builds on the previous parameterization results (Berloff, 2005a; Porta Mana and Zanna, 2014; Zanna et al., 2017; Berner et al., 2017; Cotter et al., 2018; Berloff, 2018), and prepares ground for developing data-driven stochastic eddy parameterization, for use in low-resolution ocean models. The main differences between the presented approach and past studies are in the treatment of the high-resolution data.

Our study proposes a general systematic approach to augment the low-resolution oceanic model with the forcing representing unresolved

---

* Corresponding author.
E-mail addresses: e.ryzhov@imperial.ac.uk (E.A. Ryzhov), dkondras@atmos.ucla.edu (D. Kondrashov), n.agarwal17@imperial.ac.uk (N. Agarwal),
p.berloff@imperial.ac.uk (P.S. Berloff).

small-scale dynamics. We consider a double-gyre model (Section 2), in which solutions obtained with different grid resolutions are characterized by profound differences (Section 3) both in point-wise statistics (Section 3.1) and large-scale low-frequency variability (Section 3.2). The eddy forcing is inferred from decomposition of the high-resolution solution into large- and small-scale (eddy) components and by estimating the dynamical contribution of the latter (Section 4). Augmentation of the low-resolution model with this eddy forcing substantially improves the solution towards the reference high-resolution truth (Section 5). Conclusions and discussion of the results follow in Section 6.

2. Double-gyre model

The model is the same as in Kondrashov and Berloff (2015), and here we describe it only briefly. The governing equations describe evolution of the quasi-geostrophic (QG) potential vorticity (PV) in 3 stacked isopycnal layers ($i = 1..3$ from top to bottom) with densities ρ_i ($\rho_1 = 1000$, $\rho_2 = 1001.498$, $\rho_3 = 1001.62$ kg m^{-3}) and heights H_i ($H_1 = 250$, $H_2 = 750$, $H_3 = 3000$ m):

$$\frac{\partial q_i}{\partial t} + J(\psi_i, q_i) + \beta \frac{\partial \psi_i}{\partial x} = \frac{W(x,y)}{\rho_i H_i} \delta_{1i} - \gamma \Delta \psi_i \delta_{3i} + \nu \Delta^2 \psi_i, \tag{1}$$

where q_i is the PV anomaly, ψ_i is the velocity streamfunction, $J(\cdot, \cdot)$ is the Jacobian operator, δ_{ij} is the Kronecker delta, Δ is the horizontal Laplacian operator, $\beta = 2 \cdot 10^{-11}$ m^{-1} s^{-1} is the planetary vorticity gradient, ν is the eddy viscosity (its values are further specified for different spatial resolutions), $\gamma = 4 \cdot 10^{-8}$ s^{-1} is the bottom friction parameter. The basin is square: $-L \leq x, y \leq L$, and the length of each side is $2L = 3840$ km.

The flow is forced at the surface by the stationary asymmetric wind stress curl,

$$W(x,y) = \begin{cases} -\dfrac{\pi \tau_0 A}{L} \sin \dfrac{\pi(L+y)}{L+Bx}, & y \leq Bx, \\ \dfrac{\pi \tau_0}{LA} \sin \dfrac{\pi(y-Bx)}{L-Bx}, & y > Bx, \end{cases} \tag{2}$$

where the asymmetry parameter is $A = 0.9$, the tilt parameter is $B = 0.2$, and the wind stress magnitude is $\tau_0 = 0.8$ N m^{-2}.

The PV anomaly can be inverted to obtain the streamfunctions, according to:

$$\begin{aligned} q_1 &= \Delta \psi_1 + S_1(\psi_2 - \psi_1), \\ q_2 &= \Delta \psi_2 + S_{21}(\psi_1 - \psi_1) + S_{22}(\psi_3 - \psi_2), \\ q_3 &= \Delta \psi_3 + S_3(\psi_2 - \psi_3), \end{aligned} \tag{3}$$

where the stratification parameters S_1, S_{21}, S_{22}, S_3 (corresponding to ρ_i and H_i) are such, that the first and second baroclinic Rossby deformation radii are 40 and 23 km, respectively. The boundary conditions are no-flow-through and partial-slip (with the partial-slip length scale equal to 120 km), and the mass conservation constraint is imposed in each layer.

The model produces a classical double-gyre flow pattern, characterized by a well-developed and turbulent eastward jet extension of the western boundary currents with its adjacent recirculation zones. The model solutions crucially depend on the spatial grid resolution; e.g., see Shevchenko and Berloff (2015). When the eddies are not properly resolved, the eastward jet extension weakens, shortens and becomes less coherent. The eddy feedback that sustains the eastward jet extension in the eddy-resolving regime is referred to as the backscatter process (Shevchenko and Berloff, 2016; Berloff, 2018).

The next section addresses the fundamental differences between the low- and high-resolution solutions of the model.

3. Statistical differences between the low- and high-resolution solutions

3.1. Overview

A comprehensive study of the resolution and Reynolds number dependencies of the QG double gyres is in Shevchenko and Berloff (2015). Here, we focus only on two horizontal grid resolutions: the low-resolution grid 129^2 (which corresponds to the physical grid scale of $\sim$ 30 km); and the high-resolution grid 513^2 (which corresponds to $\sim$ 7.5 km and allows for reliable resolution of the first baroclinic Rossby radius). The low- and high-resolution solutions are obtained with $\nu = 50$ and 2 m^2 s^{-1}, respectively. The larger value of ν in the low-resolution model is necessary to regularize solutions and resolve the viscous western boundary layer. Thus, the low-resolution model mishandles the small scales for 3 reasons: (1) scales smaller than the grid interval are simply not taken into account; (2) scales corresponding to several grid intervals have misrepresented dynamics due to the numerical errors; and (3) the above scales are also more damped.

For each solution the model is spun up for 100 years, until it reaches the statistical equilibrium; then, over 30k days the daily output is saved for further analyses. Fig. 1 illustrates the main differences between the low- and high-resolution circulations. A well-developed meandering eastward jet and its ambient eddy variability are clearly seen in the high-resolution flow and not seen in the low-resolution one.

3.2. Spectral analysis by Data-Adaptive Harmonic Decomposition (DAHD)

The DAHD methodology (Chekroun and Kondrashov, 2017; Kondrashov et al., 2018a) is a novel spectral analysis framework for multiscale spatio-temporal datasets. It yields a set of spatial Data-Adaptive Harmonic Modes (DAHMs) operating with individual temporal frequencies. This allows to avoid mixing temporal scales along with retaining high spectral resolution. DAHD is more appropriate than a spatio-temporal Fourier analysis, when dealing with coherent features of spatially inhomogeneous turbulence, because DAHMs are not imposed but fit empirically for the given data.

The utility of DAHD has been demonstrated for such complicated geophysical datasets, as large-scale oceanic variability (Kondrashov et al., 2018a), solar wind-magnetosphere interactions (Kondrashov and Chekroun, 2018), and sea ice conditions (Kondrashov et al., 2018b). Here, the main novelty is in applying DAHD to the eddying circulation (Fig. 1c, f).

Next is a brief introduction of DAHD, following Chekroun and Kondrashov (2017) and Kondrashov et al. (2018a). Let $\boldsymbol{X}(t_n) = \left(X_1(t_n), \dots, X_d(t_n) \right)$ with $n = 1, \dots, N$ be a multivariate time series formed of d evenly sampled spatial channels. Then, for a given pair of channels p and q, we calculate the double-sided cross-correlation coefficients $\rho_k^{(p,q)}$, characterized by time lag k (in sampling intervals) such that $-(M-1) \leq k \leq M-1$. The size of temporal embedding window M (not to be confused with the spatial averaging window W used in the following sections) should be larger than the typical decorrelation time scale in the data, and $M' = 2M - 1$ is the slowest time scale captured by DAHD.

By combining all the time-lagged cross-correlation coefficients, we construct the cross-correlation Hankel matrix $\boldsymbol{H}^{(p,q)}$, which is symmetric and obtained by left shifts of the row vector $(\rho_{-M+1}^{(p,q)}, \dots, \rho_0^{(p,q)}, \dots, \rho_{M-1}^{(p,q)})$, so that every anti-diagonal consists of the same elements.

Then, by arranging all $\boldsymbol{H}^{(p,q)}$ for each pair of channels (p, q), we obtain the block-Hankel matrix:

$$\begin{aligned} \boldsymbol{C}^{(p,q)} &= \boldsymbol{H}^{(p,q)}, & p \leq q, \\ \boldsymbol{C}^{(p,q)} &= \boldsymbol{H}^{(q,p)}, & \text{elsewhere} \end{aligned} \tag{4}$$

Block-matrix $\boldsymbol{C}$ consists of d^2 ($p = 1, \dots, d$, $q = 1, \dots, d$) blocks of size $(2M-1)^2$ each. An important property is that eigenvalues of $\boldsymbol{C}$ come in pairs of opposite values but with opposite sign. Moreover,
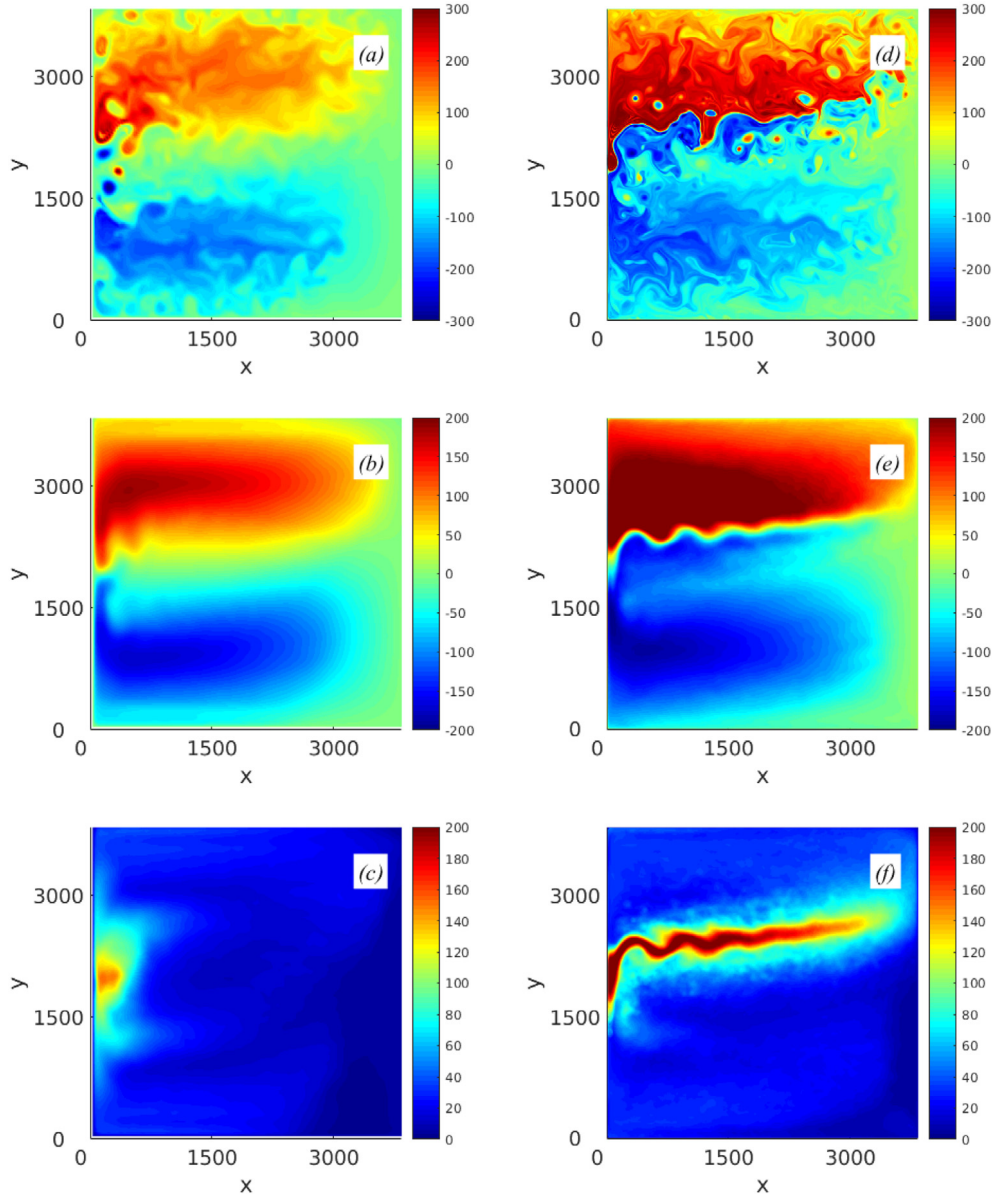
Fig. 1. The main nonlinear effect of the eddies: amplification of the eastward jet and its adjacent recirculation zones. PV anomaly maps of the double-gyre upper-ocean reference circulations: left column of panels shows the low-resolution (129^2) solution; right column of panels shows the high-resolution (513^2) solution. (a), (d) — instantaneous snapshots of the flow; (b), (e) — time means; (c), (f) — standard deviations. The colour scale units are nondimensional (with the length scale being the grid interval and the velocity scale 0.01 m/s) and the same across the figures. Solutions in the deep layers are not shown for brevity, but they convey essentially the same message.

these eigenvalues can be attributed to the corresponding single temporal frequencies characterizing the corresponding eigenvectors $\mathbf{W}_j = (\mathbf{E}_1^j, \ldots, \mathbf{E}_d^j)$. Here, $\mathbf{E}_k^j$ is an M'-long row vector, which can be expressed as

$$\mathbf{E}_k^j(s) = B_k^j \cos(2\pi f s + \theta_k^j), \quad 1 \le s \le M'; \quad 1 \le k \le d, \tag{5}$$

where the amplitudes B_k^j and phases θ_k^j are data-adaptive, while frequency f is equally spaced in Nyquist interval [0 0.5] with M values:

$$f = \frac{(\ell - 1)}{M' - 1}, \quad \ell = 1, \ldots, \frac{M' + 1}{2} \tag{6}$$

In total, $j = 1, \ldots, d(2M - 1)$ spectral eigenelements $(\lambda_j, \mathbf{W}_j)$ are computed, and there are exactly d eigenvalue pairs associated with each frequency $f \ne 0$, while there are d unpaired eigenvalues corresponding to $f = 0$.

By plotting the eigenvalues $|\lambda_j|$ according to the frequencies f of corresponding DAHMs, we obtain the DAHD power spectrum. By using

the largest possible embedding window $M = N/2$, we obtain the best possible frequency resolution and also representation of the lowest available frequencies.

We applied DAHD to the upper-ocean PV anomaly daily fields of the reference solutions (Section 3). To make our analyses computationally efficient, first, we compressed these fields by applying a standard principal component analysis (PCA) (Preisendorfer, 1988) and retaining the leading $d = 2000$ empirical orthogonal function (EOF) modes. These modes captured nearly all variance in the low- and high-resolution simulations: 98% and 95%, respectively. Next, we projected the original PV anomaly fields on the retained EOFs, and, thus, obtained the corresponding principal components (PCs). These PCs constitute $d = 2000$ time series used as the input for DAHD analyses.

To have both the adequate spectral resolution and the low-frequency part of the spectrum, we considered 30k days long PCs, sub-sampled every 5 days. Thus, we have $N = 6000$ samples and use the largest possible embedding window with width $M = N/2 = 3000$ (i.e., $M' = 5999 \approx 80$ years). However, these values of M and d yield C of size
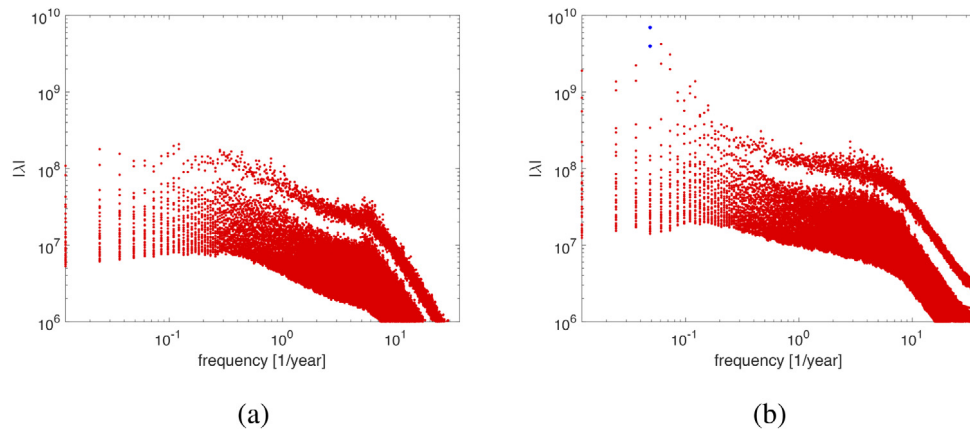
Fig. 2. Temporal spectral content of the reference solutions: (a) 129^2, (b) 513^2 grids. Leading part of DAHD power spectrum (30 largest values of $|\lambda|$ are shown at each frequency) of the upper-layer PV anomalies. Blue dots in panel (b) correspond to the interdecadal variability peak at ≈ 20 years; this variability is absent in the low-resolution solution corresponding to panel (a).

$\approx 10^7 \cdot 10^7$, which renders its direct eigendecomposition computationally prohibitive.

Following results of earlier studies (Chekroun and Kondrashov, 2017; Kondrashov et al., 2018a), we thus rely on alternative and computationally efficient way to calculate DAHD eigenvalues by using a singular value decomposition (SVD) of $d \times d$ cross-spectral matrix $\mathfrak{S}(f)$:

$$\mathfrak{S}_{p,q} = \begin{cases} \widehat{\rho^{p,q}}(f) & \text{if } q \geq p, \\ \widehat{\rho^{q,p}}(f) & \text{if } q < p, \end{cases} \tag{7}$$

where $1 \leq p, q \leq d$, and $\widehat{\rho^{p,q}}(f)$ is the Fourier transform of the cross-correlation $\rho_k^{(p,q)}$ time series in the embedding space, i.e. $-(M-1) \leq k \leq M-1$.

Theorem V.1 of Chekroun and Kondrashov (2017) establishes that for each singular value $\sigma_p(f)$ of $\mathfrak{S}(f)$ there exists, when $f \neq 0$, a pair of opposite eigenvalues $(\lambda_-^p(f), \lambda_+^p(f))$ of C, such that:

$$\lambda_+^p(f) = -\lambda_-^p(f) = \sigma_p(f), \qquad 1 \leq p \leq d, \tag{8}$$

i.e., there are $2d$ eigenvalues associated with each frequency. The same theorem also states that there are only d unpaired eigenvalues corresponding to $f = 0$. Additional advantage of using SVD of $\mathfrak{S}(f)$ for computing the set of λ is that it can be done in parallel for each frequency, i.e., it is computationally efficient (even laptop-enabled).

Fig. 2 compares the DAHD power spectra of the reference solutions: overall, the shapes of the spectra are similar and characterized by the band of higher values separated by a small gap from the broadly distributed band of lower values. The spectral band of higher values corresponds to the most energetic DAHMs, which dominate the solution. A power law dependence in the high-frequency part is found by fitting a straight line in the corresponding log–log plot.

The low-resolution solution spectrum has significantly smaller magnitudes, which is in agreement with the reduced eddy activity. Furthermore, only the high-resolution solution is characterized by significant low-frequency variability (LFV) corresponding to the dominant spectral power peak at ≈ 20 years. This interdecadal LFV was studied elsewhere (Berloff and McWilliams, 1999; Berloff et al., 2007; Shevchenko et al., 2016), and here we just note that a well-augmented low-resolution model should aim to recover it.

4. Eddy forcing inference from the high-resolution solutions

Our main goal is to dynamically augment the low-resolution model, so that its solution recovers the key features of the high-resolution solution: the eastward jet extension and its adjacent recirculation zones, and the interdecadal LFV (Figs. 1 and 2).

First, we need to address the dynamics missing from the low-resolution model. Generally speaking, one may assume, that low-resolution models are capable of resolving slowly varying large-scale dynamics but fail to resolve more transient small-scale dynamics, whereas high-resolution models resolve everything. The caveat here is that the low-resolution model can still need an augmentation to realize its capability. As a preliminary step, we assume that the low- and high-resolution large-scale dynamics are similar and implement a decomposition of the high-resolution fields of interest, that is, streamfunction Ψ and PV anomaly Q (in general notation, without layer indexing):

$$\Psi = \overline{\Psi} + \Psi', \quad Q = \overline{Q} + Q', \tag{9}$$

where overbar indicates large-scale component and prime indicates small-scale (eddy) component. All the fields vary in time and space. Note, that the decomposition is somewhat arbitrary and not objectively constrained, and in practice it is not unique (Hasselmann, 1988; von Storch et al., 1995; Schmid, 2010; Li and von Storch, 2013; Dijkstra, 2013, 2018; Viebahn et al., 2019), which is a problematic issue.

By substituting (9) into the governing equation (1) rewritten in terms of material derivative of the large-scale flow component, we obtain the following equation that couples the large-scale and eddy dynamics:

$$\frac{\partial \overline{Q}}{\partial t} + J(\overline{\Psi}, \overline{Q}) = \mathcal{F}\left(\overline{\Psi}, \overline{Q}, \Psi', Q'\right) + \mathcal{H}(\overline{\Psi}, \overline{Q}) + \mathcal{L}(\Psi' Q'), \tag{10}$$

where the operator $\mathcal{H}$ contains all the nonconservative terms involving only the large-scale components, the linear operator $\mathcal{L}$ contains the eddy tendency term and all the nonconservative terms involving only the eddy components, whereas the remaining term,

$$\mathcal{F} = -\left(J(\overline{\Psi}, Q') + J(\Psi', \overline{Q}) + J(\Psi', Q')\right), \tag{11}$$

is the eddy forcing (Berloff, 2005a) exerted by the nonlinear coupling between the eddy and large-scale flow components, as well as by the eddy nonlinearity. The linear eddy term $\mathcal{L}$ can be neglected, because we found that its contribution is about 2% of that of the eddy forcing.

For decomposition (11) implemented on the high-resolution grid, we apply the simplest technique – a spatial moving-average filter – and extract the large-scale flow component; the small-scale component is obtained as the residual. The averaging window is taken to be of the order of the first baroclinic Rossby deformation radius; it is a square window with the side of $W = 21$ high-resolution grid intervals (which corresponds to physical scale of ~ 150 km). The filter is applied to the layer-wise streamfunction, and the corresponding PV anomaly is obtained from (3); the layer-wise eddy forcing $\mathcal{F}$ is found from (11) and then coarse-grained onto 129x129 low-resolution grid.
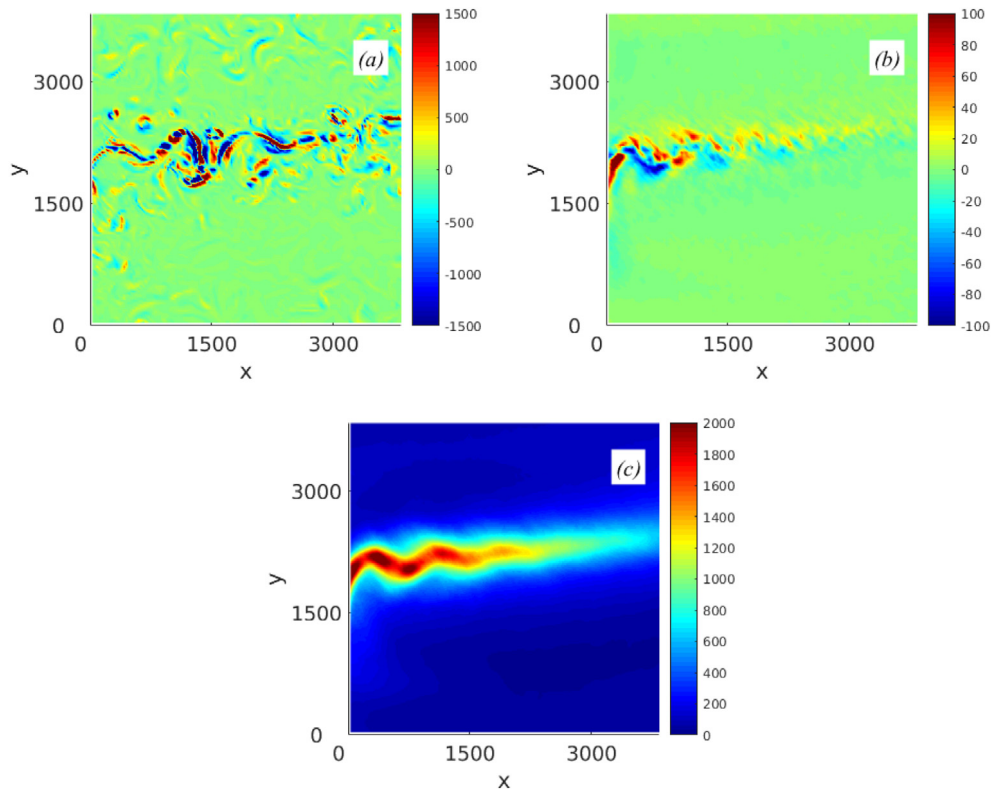
Fig. 3. Spatial structure of the eddy forcing $\mathcal{F}$ in the upper layer. Inferred upper-layer $\mathcal{F}_\infty$: (a) an instantaneous snapshot; (b) the mean; (c) the standard deviation.

Fig. 3 illustrates typical features of the inferred eddy forcing. Over-all, the eddy forcing is most intense around the eastward jet; its time mean is small relative to the fluctuations, and its spatial pattern is complicated and characterized by small-scale features. It is worth noting that $\mathcal{F}$ is typically more intense for larger averaging windows, which result in more intense eddies, whereas relative changes of the large-scale flow component are modest.

Next, we applied DAHD to analyse the spatio-temporal structure of the eddy forcing. Similar to the analysis of PV anomaly (Section 3), first, we applied PCA to the daily dataset of $\mathcal{F}$ and retained the leading $d = 2000$ PCs, which capture 90% of the variance. Then we applied DAHD to the dataset composed of these PCs, using the embedding window of $M = 3000$ days. The resulting DAHD power spectrum is such that 10 largest values of $|\lambda|$ are organized in the red-noise background distribution, but there is also sharp peak of power at zero frequency (see Fig. 4) that accounts for the modulation of the eddy forcing intensity at very slow time scales. We argue that the latter yields the corresponding interdecadal LFV peak in the high-resolution reference spectrum solution (Fig. 2.)

Our next step is to augment the low-resolution model with the inferred eddy forcing $\mathcal{F}$, so that it simulates a significantly improved solution.

5. Augmentation of the low-resolution model by inferred eddy forcing

As a first step, the 30k days long record of raw $\mathcal{F}$ was added to the right-hand side of the low-resolution model and looped around. Then, the model was spun up for several years and after that integrated for 30k days, with the solution output saved for further analyses. While the eastward jet in the augmented solution is restored, its shape is blurred and poorly resembles the reference high-resolution truth (compare Figs. 5 and 1). The difference is especially conspicuous in the region
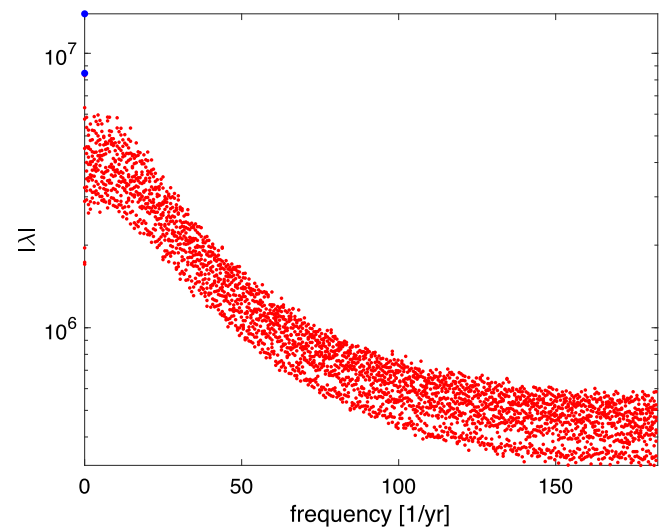

Fig. 4. Spectral content of the eddy forcing. Leading part of the DAHD power spectrum (shown are 10 largest $|\lambda|$ at each frequency) of the upper-layer eddy forcing inferred from the reference high-resolution solution. A sharp peak at zero frequency (blue dots) accounts for the modulation of the eddy forcing intensity at very slow time scales.

where the eastward jet separates from the western boundary. To fix this problem the inferred $\mathcal{F}$ has to be modified to be dynamically more consistent with the low-resolution model. In particular, the fact that the low-resolution model partially resolves the nonlinear dynamics responsible for maintaining the eastward jet extension should be taken into account.
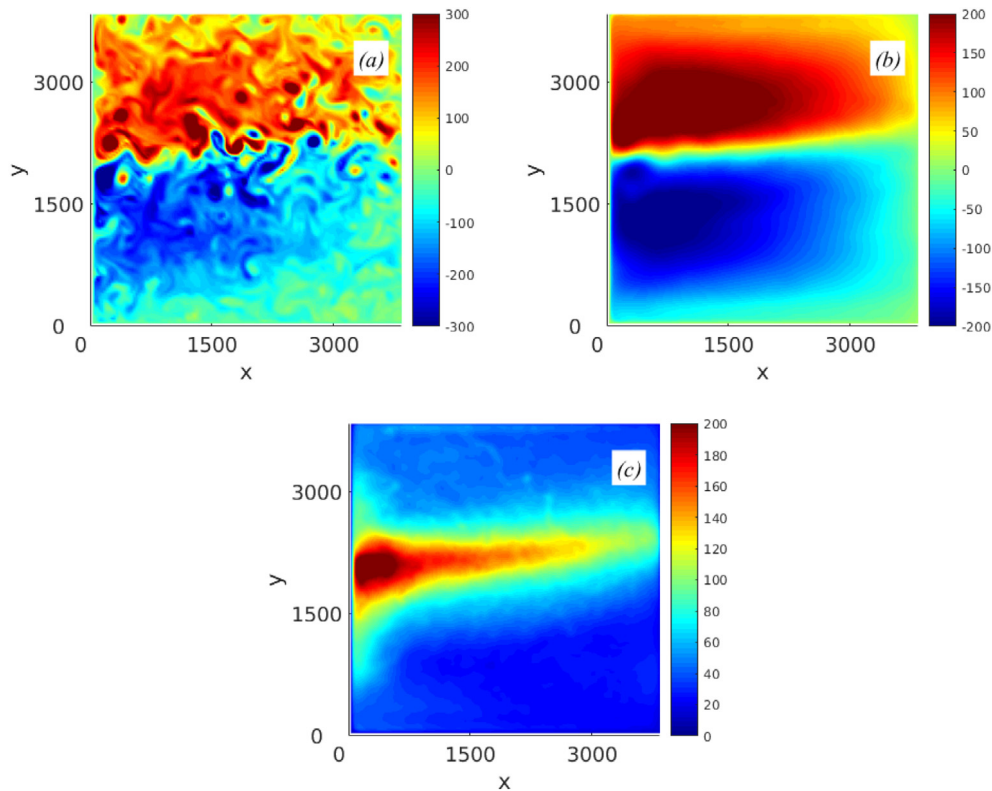
Fig. 5. Low-resolution model solution augmented with the unconstrained eddy forcing. Statistical characteristics of the upper-layer PV anomaly: (a) an instantaneous snapshot; (b) the mean; (c) the standard deviation. Compare this solution with Fig. 1 and note that while there is obvious improvement towards the high-resolution truth, the eastward jet is characterized by excessive variability, especially in the upstream region.
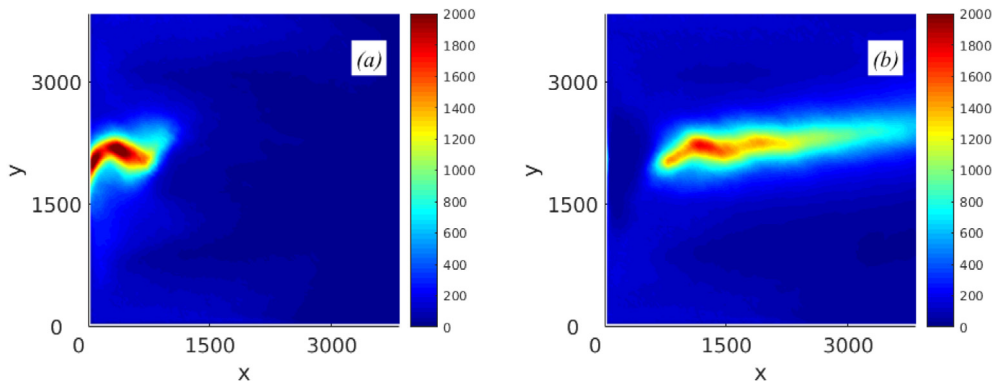

Fig. 6. Constraining eddy forcing by taking into account partially resolved eddy dynamics. Standard deviations of the upper-layer eddy forcing components: (a) the excess forcing $\mathcal{F}_{LR}$; (b) the modified eddy forcing $\mathcal{F}_{mod}$ obtained by removing the excess forcing. Compare with Fig. 3b, which shows the raw eddy forcing.

We achieve dynamically-consistent eddy forcing by considering the low-resolution model solutions of streamfunction Ψ_{LR}, potential vorticity Q_{LR} and Jacobian $J_{LR}(\Psi_{LR}, Q_{LR})$. The spatio-temporal structure of J_{LR} provides us with information on resolved dynamics in the low-resolution model, that is statistically removed from the eddy forcing $\mathcal{F}$. First, we apply PCA to decompose the spatio-temporal field of J_{LR}, and retain 2000 EOFs that capture 99% of its variance. Then $\mathcal{F}$ (that has the same temporal length 30 K days and spatial size 129^2 as J_{LR}) is projected onto this set of EOFs, and subsequently reconstructed in time and space to diagnose corresponding spatio-temporal field $\mathcal{F}_{LR}$ (Fig. 6), which is then subtracted from $\mathcal{F}$ to obtain spatio-temporal field of modified forcing $\mathcal{F}_{mod} = \mathcal{F} - \mathcal{F}_{LR}$.

With the modified forcing $\mathcal{F}_{mod} = \mathcal{F} - \mathcal{F}_{LR}$ imposed, the excessive variability in the upstream part of the eastward jet is largely suppressed, and the solution is improved (Fig. 7); the apparent improvements can be seen by comparing with the low- and high-resolution

reference solutions (Fig. 1). From now on, we will refer to the constrained augmented solution as the *reference augmented solution*. The reference augmented flow develops a lot more eddies and resembles the eddy-resolving reference solution. These eddies couple with the evolving eastward jet and enhance it (most likely via the backscatter mechanism (Berloff, 2018), but the proper analysis will be included in a separate paper). Furthermore, the mean and standard deviation fields attest that the geometrical structure of the flow statistics is also significantly improved (Fig. 7). On the other hand, the eastward jet in the reference augmented solution (Fig. 7c) is broader and less coherent than in the eddy-resolving truth (Fig. 1f). The other noticeable difference is that the augmented large-scale subtropical and subpolar gyres are moderately weaker than the eddy-resolving truth; in other words the augmentation amplified (relatively weak) counter-rotating gyre anomalies (Shevchenko and Berloff, 2016). Understanding the underlying mechanisms of this secondary effect is beyond the limited
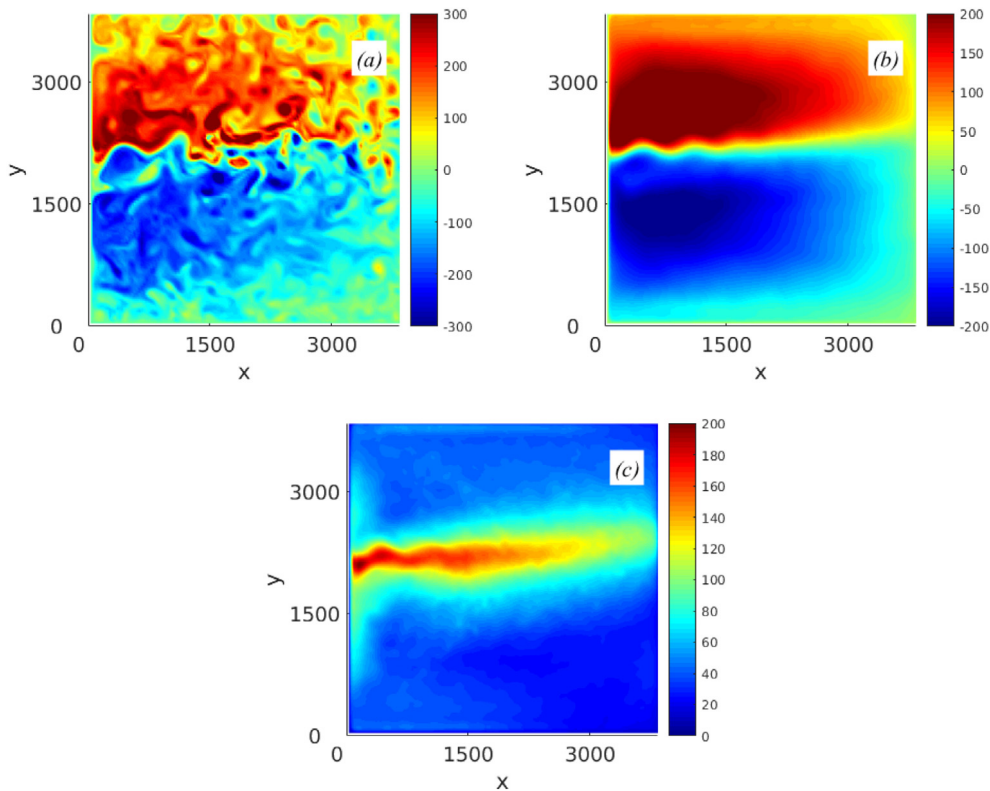
Fig. 7. Reference augmented (low-resolution) solution with dynamically constrained eddy forcing. Statistical characteristics of the upper-layer PV anomaly: (a) an instantaneous snapshot; (b) the mean; (c) the standard deviation. Compare this with Fig. 5 illustrating the unconstrained case and with Fig. 1 showing the non-augmented reference solutions.
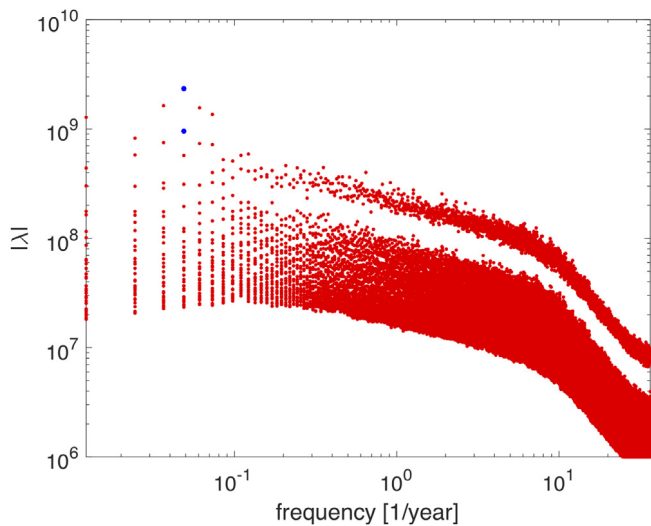

Fig. 8. Spectral content of the reference augmented (low-resolution) solution. The leading part of the DAHD power spectrum (shown are 30 largest $|\lambda|$ at each frequency) of the upper-layer PV anomaly. The prominent peak at $\approx$ 20 years (blue dots) corresponds to the LFV, which is structurally similar to the reference one obtained in the high-resolution solution (Fig. 2b).

goals of this paper, but we speculate that this is because of the inconsistencies between the imposed eddy forcing and the large-scale flow response, which enhance material transport across the eastward jet and, thus, reduce the PV contrast between the gyres.

We analysed the DAHD spectrum to continue assessment of the quality of the reference augmented solution. A key problem of the unconstrained augmented low-resolution solution is the absence of the LFV. In contrast, the reference augmented solution recovers the LFV,

albeit it is less intensive (Fig. 8; compare with Fig. 2). Overall, the shape and magnitude of the DAHD spectrum are well reproduced. The patterns of the leading LFV EOFs are also captured qualitatively well (not shown). To summarize, the augmented reference solution is characterized by significant improvement of not only the spatial flow structure but also the LFV characteristics. By considering the latter property, we add a quality requirement for assessing the performance of the upcoming parameterization.

As mentioned above, the eddy forcing is not unique and depends on the flow decomposition into a combination of large- and small-scale components. Complete analysis of the sensitivity to the decomposition, as well as the search for objective and optimal decompositions, remains beyond the scope of this paper. However, we studied the dependence of the augmentation on the averaging filter width W, by considering filters with the shorter $W = 11$ (corresponds to $\sim$ 75 km in the physical scale) and the longer $W = 31$ ($\sim$ 225 km). Relative to the reference case with $W = 21$, the augmented solutions with $W = 11$ and $W = 31$ produce underpredicted and overpredicted eastward jet extensions, respectively (Fig. 9), and the corresponding DAHD spectra are characterized by the lower and higher magnitudes, respectively (not shown), which is consistent with the differences in eddy intensity. From this we conclude that for a non-eddy-resolving grid, with the nominal resolution about half of the first baroclinic Rossby deformation radius, the optimal flow decomposition scale is about 4 deformation radii. In other words, the augmentation allows to coarsen the grid by an order of magnitude, which is quite encouraging.

6. Conclusions and discussion

We have presented a general data-driven approach on augmenting low-resolution ocean circulation models with a specifically tailored extra (eddy) forcing that represents eddy feedbacks, which cannot be properly resolved. The eddy forcing is inferred diagnostically by decomposing the high-resolution model solution, which is treated as the
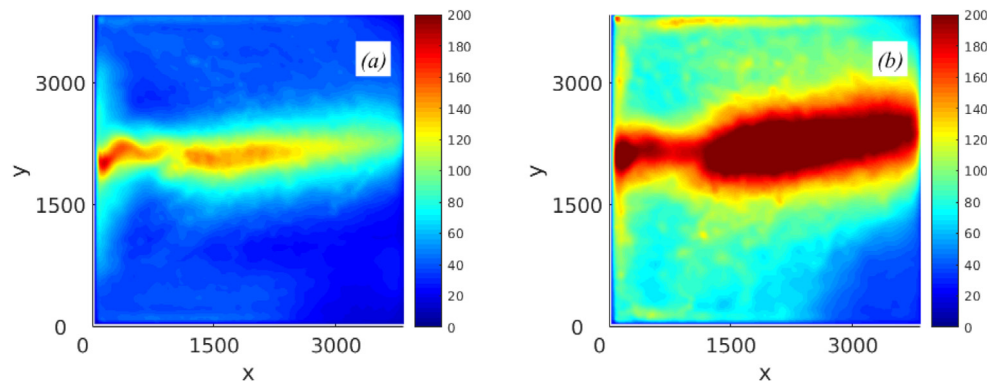
E.A. Ryzhov, D. Kondrashov, N. Agarwal et al.

Ocean Modelling 142 (2019) 101464

Fig. 9. Dependence of the augmented solution on the decomposition filter width. Standard deviation of the upper-layer PV anomaly from the reference augmented solution based on the averaging window: (a) $W = 11$ (corresponds to 75 km); (b) $W = 31$ (225 km). Compare with Fig. 7c illustrating the outcome of a more optimal filter width.

available data, into a combination of large- and small-scale flow components (both are spatio-temporal fields). The forcing, first, is applied as it is, but, then, it is modified to be dynamically consistent with the low-resolution model. For this we applied the novel method utilizing spatio-temporal characteristics of the low-resolution Jacobian operator (i.e., nonlinear advection term) and removes the "double counting" effect due to partially resolved eddies of the low-resolution dynamics. We refer to this method as the *constrained augmentation*. The geometrical shape of the eastward jet extension and its adjacent recirculation zones, as well as the interdecadal low-frequency variability (LFV) of the constrained augmented solution are significantly improved towards the eddy-resolving truth.

Our results can be extended in several directions. First, feedback from the low-resolution model can be interactively incorporated into online calculation of the eddy forcing (e.g., as in Berloff, 2005a), provided that the eddy field is statistically emulated based on the available data (Kravtsov et al., 2005; Kondrashov and Berloff, 2015; Kondrashov et al., 2018a). In this case the coupling between eddy and large-scale dynamics should be more consistent. In the meantime, we explored the eddy forcing extracted from the high-resolution data, assuming that the large-scale flow component is indeed an accurate solution of the low-resolution model, which is not necessarily the case. A related issue concerns the consistency of the applied flow decomposition. More focused research into effects of scale-adaptive decompositions, which have a spatial filter width (and even shape) depending on the local spatial correlation radius may improve quality of the augmented low-resolution model. Treating temporal filtering in a similar way is also on the wish-list.

The utility of a long record of the eddy forcing, as in the present study, is unclear and should be studied separately. We hypothesize that only short-time variability of the eddy forcing actually matters, and, if true, this will justify shorter statistical emulations of the eddies. The question of augmenting models with incomplete or noisy data is big, problematic, and completely left out for separate studies. Finally, extending the approach presented in this paper, as well as its obvious extensions mentioned above, to the comprehensive general circulation models written in terms of primitive equations will be a practical step forward.

Acknowledgements

References

Abernathey, R., Haller, G., 2018. Transport by Lagrangian vortices in the eastern pacific. J. Phys. Oceanogr. 48, 667–685.

Bachman, S.D., 2019. The GMiiijŃE closure: A framework for coupling backscatter with the gent and mcwilliams parameterization. Ocean Model. 136, 85–106.

Berloff, P., 2005a. On dynamically consistent eddy fluxes. Dyn. Atmos. Ocean 38, 123–146.

Berloff, P., 2005b. Random-forcing model of the mesoscale oceanic eddies. J. Fluid Mech. 529, 71–95.

Berloff, P., 2018. Dynamically consistent parameterization of mesoscale eddies. part III: deterministic approach. Ocean Model. 127, 1–15.

Berloff, P., Hogg, A., Dewar, W., 2007. The turbulent oscillator: A mechanism of low-frequency variability of the wind-driven ocean gyres. J. Phys. Oceanogr. 37, 2363–2386.

Berloff, P.S., McWilliams, J., 1999. Large-scale, low-frequency variability in wind-driven ocean gyres. J. Phys. Oceanogr. 29, 1925–1949.

Berner, J., Achatz, U., Batté, L., Bengtsson, L., Cámara, A., et al., 2017. Stochastic parameterization: Toward a new view of weather and climate models. Bull. Amer. Meteorol. Soc. 98 (3), 565–588.

Chekroun, M.D., Kondrashov, D., 2017. Data-adaptive harmonic spectra and multilayer stuart-landau models. Chaos 27, 093110.

Chelton, D.B., Schlax, M.G., Samelson, R.M., 2011. Global observations of nonlinear mesoscale eddies. Prog. Oceanogr. 91 (2), 167–216.

Chelton, D.B., Schlax, M.G., Samelson, R.M., de Szoeke, R.A., 2007. Global observations of large oceanic eddies. Geophys. Res. Lett. 34, L15606.

Cotter, C., Crisan, D., Holm, D.D., Wei Pan, Shevchenko, I., 2018. Modelling uncertainty using circulation-preserving stochastic transport noise in a 2-layer quasi-geostrophic model, ArXiv.

Crommelin, D., Vanden-Eijnden, E., 2008. Subgrid-scale parameterization with conditional Markov chains. J. Atmos. Sci. 65 (8), 2661–2675.

Danilov, S., Juricke, S., Kutsenko, A., Oliver, M., 2019. Toward consistent subgrid momentum closures in ocean models. In: Energy Transfers in Atmosphere and Ocean. Springer International Publishing, pp. 145–192.

Dijkstra, H.A., 2013. Nonlinear Climate Dynamics. Cambridge University Press, Cambridge, UK.

Dijkstra, H.A., 2018. A normal mode perspective of intrinsic ocean-climate variability. Annu. Rev. Fluid Mech. 48, 341–363.

Dong, C., McWilliams, J.C., Liu, Y., Chen, D., 2014. Global heat and salt transports by eddy movement. Nature Commun. 5, 3294.

Frederiksen, J.S., 1999. Subgrid-scale parameterizations of eddy-topographic force, eddy viscosity, and stochastic backscatter for flow over topography. J. Atmos. Sci. 56 (11), 1481–1494.

Frederiksen, J.S., Davies, A.G., 1997. Eddy viscosity and stochastic backscatter parameterizations on the sphere for atmospheric circulation models. J. Atmos. Sci. 54 (20), 2475–2492.

Frederiksen, J.S., O´Kane, T.J., Zidikheri, M.J., 2012. Stochastic subgrid parameterizations for atmospheric and oceanic flows. Phys. Scr. 85 (6), 068202.

Gent, P.R., McWilliams, J.C., 1990. Isopycnal mixing in ocean circulation models. J. Phys. Oceanogr. 20 (1), 150–155.

Griffies, S.M., Böning, C., Bryan, F.O., Chassignet, E.P., Gerdes, R., Hasumi, H., Hirst, A., Treguier, A.-M., Webb, D., 2000. Developments in ocean climate modelling. Ocean Model. 2 (3), 123–192.

Grooms, I., Majda, A.J., Smith, K.S., 2015. Stochastic superparameterization in a quasigeostrophic model of the antarctic circumpolar current. Ocean Model. 85, 1–15.

Hasselmann, K., 1988. PIPs and POPs: The reduction of complex dynamical systems using principal interaction and oscillation patterns. J. Geophys. Res.: Atmos. 93 (D9), 11015–11021.

Holloway, G., 1987. Systematic forcing of large-scale geophysical flows by eddy-topography interaction. J. Fluid Mech. 184, 463–476.

Jansen, M.F., Held, I.M., 2014. Parameterizing subgrid-scale eddy effects using energetically consistent backscatter. Ocean Model. 80, 36–48.

Jansen, M.F., Held, I.M., Adcroft, A., Hallberg, R., 2015. Energy budget-based backscatter in an eddy permitting primitive equation model. Ocean Model. 94, 15–26.

Juricke, S., Danilov, S., Kutsenko, A., Oliver, M., 2019. Ocean kinetic energy backscatter parametrizations on unstructured grids: Impact on mesoscale turbulence in a channel. Ocean Model. 138, 51–67.

Kitsios, V., Frederiksen, J., Zidikheri, M., 2013. Scaling laws for parameterisations of subgrid eddy–eddy interactions in simulations of oceanic circulations. Ocean Model. 68, 88–105.

Kondrashov, D., Berloff, P., 2015. Stochastic modeling of decadal variability in ocean gyres. Geophys. Res. Lett. 42, 1543–1553.

Kondrashov, D., Chekroun, M.D., 2018. Data-adaptive harmonic analysis and modeling of solar wind-magnetosphere coupling. J. Atmos. Sol.-Terr. Phys..

Kondrashov, D., Chekroun, M.D., Berloff, P., 2018a. Multiscale stuart-landau emulators: Application to wind-driven ocean gyres. Fluids 3, 21.

Kondrashov, D., Chekroun, M.D., Ghil, M., 2018b. Data-adaptive harmonic decomposition and prediction of arctic sea ice extent. Dyn. Statist. Clim. Syst..

Kravtsov, S., Berloff, P., Dewar, W., Ghil, M., McWilliams, J., 2006. Dynamical origin of low-frequency variability in a highly nonlinear midlatitude coupled model. J. Clim. 19, 6391–6408.

Kravtsov, S., Kondrashov, D., Ghil, M., 2005. Multi-level regression modeling of nonlinear processes: Derivation and applications to climatic variability. J. Clim. 18, 4404–4424.

Li, H., von Storch, J.-S., 2013. On the fluctuating buoyancy fluxes simulated in a OGCM. J. Phys. Oceanogr. 43 (7), 1270–1287.

Liu, Y., Wilson, C., Green, M.A., Hughes, C.W., 2018. Gulf stream transport and mixing processes via coherent structure dynamics. J. Geophys. Res.: Oceans 123 (4), 3014–3037.

Mak, J., Maddison, J.R., Marshall, D.P., Munday, D.R., 2018. Implementation of a geometrically informed and energetically constrained mesoscale eddy parameterization in an ocean circulation model. J. Phys. Oceanogr. 48 (10), 2363–2382.

Mak, J., Marshall, D., Maddison, J., Bachman, S., 2017. Emergent eddy saturation from an energy constrained eddy parameterisation. Ocean Model. 112, 125–138.

O´Kane, T.J., Frederiksen, J.S., 2008. Statistical dynamical subgrid-scale parameterizations for geophysical flows. Phys. Scr. T132, 014033.

Porta Mana, P., Zanna, L., 2014. Toward a stochastic parametrization of ocean mesoscale eddies. Ocean Model. 79, 1–20.

Preisendorfer, R.W., 1988. Principal Component Analysis in Meteorology and Oceanography. Elsevier, New York, p. 425.

Samelson, R., 2013. Lagrangian motion, coherent structures, and lines of persistent material strain. Annu. Rev. Mar. Sci. 5 (1), 137–163, PMID: 22809180.

Samelson, R.M., Schlax, M.G., Chelton, D.B., 2016. A linear stochastic field model of midlatitude mesoscale variability. J. Phys. Oceanogr. 46 (10), 3103–3120.

Schmid, P.J., 2010. Dynamic mode decomposition of numerical and experimental data. J. Fluid Mech. 656, 5–28.

Shevchenko, I.V., Berloff, P.S., 2015. Multi-layer quasi-geostrophic ocean dynamics in eddy-resolving regimes. Ocean Model. 94, 1–14.

Shevchenko, I., Berloff, P., 2016. Eddy backscatter and counter-rotating gyre anomalies of midlatitude ocean dynamics. Fluids 1 (3).

Shevchenko, I., Berloff, P., Guerrero-Lopez, D., Roman, J., 2016. On low-frequency variability of the midlatitude ocean gyres. J. Fluid Mech. 795, 423–442.

Viebahn, J., Crommelin, D., Dijkstra, H., 2019. Toward a turbulence closure based on energy modes. J. Phys. Oceanogr. 49 (4), 1075–1097.

von Storch, H., Bürger, G., Schnur, R., von Storch, J.-S., 1995. Principal oscillation patterns: A review. J. Clim. 8 (3), 377–400.

Zacharuk, M., Dolaptchiev, S.I., Achatz, U., Timofeyev, I., 2018. Stochastic subgrid-scale parametrization for one-dimensional shallow-water dynamics using stochastic mode reduction. Q. J. R. Meteorol. Soc. 144 (715), 1975–1990.

Zanna, L., Porta Mana, P., Anstey, J., David, T., Bolton, T., 2017. Scale-aware deterministic and stochastic parametrizations of eddy-mean flow interaction. Ocean Model. 111, 66–80.

Zhang, Z., Wang, W., Qiu, B., 2014. Oceanic mass transport by mesoscale eddies. Science 345, 322–324.

Zidikheri, M.J., Frederiksen, J.S., 2010a. Stochastic modelling of unresolved eddy fluxes. Geophys. Astrophys. Fluid Dyn. 104 (4), 323–348.

Zidikheri, M.J., Frederiksen, J.S., 2010b. Stochastic subgrid-scale modelling for non-equilibrium geophysical flows. Phil. Trans. R. Soc. A 368 (1910), 145–160.